







Cite this: *Soft Matter*, 2023,  
19, 4571

## Motility-induced shear thickening in dense colloidal suspensions†

A. Gülce Bayram, <sup>a</sup> Fabian Jan Schwarzendahl, <sup>b</sup> Hartmut Löwen <sup>b</sup> and Luca Biancofiore <sup>\*a,c</sup>

Phase transitions and collective dynamics of active colloidal suspensions are fascinating topics in soft matter physics, particularly for out-of-equilibrium systems, which can lead to rich rheological behaviours in the presence of steady shear flow. Here the role of self-propulsion in the rheological response of a dense colloidal suspension is investigated by using particle-resolved Brownian dynamics simulations. First, the combined effect of activity and shear in the solid on the disordering transition of the suspension is analyzed. While both self-propulsion and shear destroy order and melt the system if critical values are exceeded, self-propulsion largely lowers the stress barrier needed to be overcome during the transition. We further explore the rheological response of the active sheared system once a steady state is reached. While passive suspensions show a solid-like behaviour, turning on particle motility fluidises the system. At low self-propulsion, the active suspension behaves in the steady state as a shear-thinning fluid. Increasing the self-propulsion changes the behaviour of the liquid from shear-thinning to shear-thickening. We attribute this to clustering in the sheared suspensions induced by motility. This new phenomenon of motility-induced shear thickening (MIST) can be used to tailor the rheological response of colloidal suspensions.

Received 10th January 2023,  
Accepted 7th June 2023

DOI: 10.1039/d3sm00035d

rsc.li/soft-matter-journal

## 1 Introduction

During the last decade, active matter has become a topic of intense research.<sup>1,2</sup> In particular, active colloids have been investigated<sup>3</sup> since they provide a well-controlled testing ground for out-of-equilibrium systems. Experimentally, one among many realizations of active particles is active Janus colloids,<sup>3</sup> which can show fascinating phenomena such as motility-induced phase separation,<sup>4,5</sup> vortex formation,<sup>6</sup> clustering induced by hydrodynamic fluxes<sup>7</sup> or wall accumulation.<sup>8–10</sup> Dense suspensions of active particles have been realized and studied experimentally for Janus colloids,<sup>11</sup> for vibrated active disks<sup>12,13</sup> and theoretically.<sup>14–16</sup> Active particles that are in a glassy state<sup>17</sup> have given insights into random close packing<sup>18</sup> and it has been shown that shearing an active glass former leads to ordering.<sup>19</sup> However, the rheological properties of dense active colloids are largely unknown.

On the side of biological microswimmers, such as bacteria or microalgae, it has been shown that the presence of a small fraction of active swimmers in a fluid medium can fundamentally change the fluid's rheological properties. It was found experimentally that pusher-type swimmers such as the bacterium *Escherichia coli* reduce the effective viscosity<sup>20–24</sup> while puller-type swimmers such as the microalgae *Chlamydomonas reinhardtii* can increase the viscosity.<sup>25</sup> This response to the swimming behavior has also been explained in theoretical and numerical studies.<sup>26–33</sup> Further, the rheological properties of active fluids, that can model driven microtubules or active actin filaments, have been computed using field theoretical approaches.<sup>33–36</sup>

Here, we investigate the rheological properties of dense active colloids in two spatial dimensions using Brownian dynamics computer simulations. Note that colloidal particles in our model are different from biological microswimmers which typically use their limbs to swim *via* mechanical motion which gives rise to long-range hydrodynamic interactions. Colloidal particles are moving in a self-generated gradient and in many cases, their hydrodynamic interactions are much smaller.<sup>37</sup> Investigating the strain–stress curves shows that activity reduces and even destroys the stress barrier that a shear flow has to overcome to fluidise the system. In the steady state, the system's shear stress reveals that particle motility fundamentally changes the rheological properties of the system: at none or low activity the system is shear thinning, for

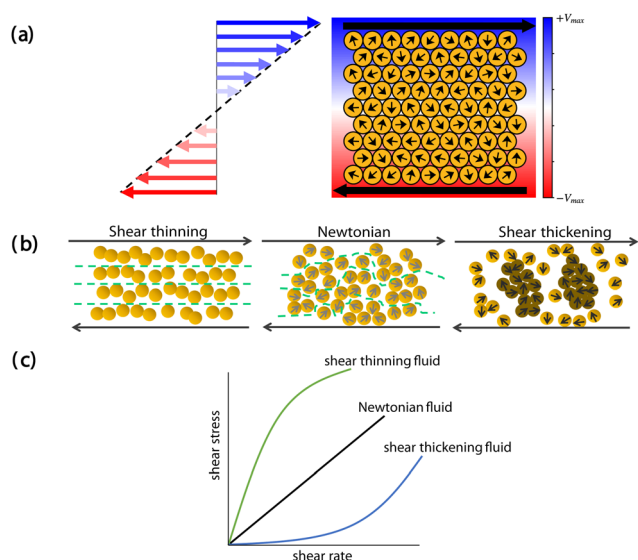
<sup>a</sup> FluidFrame Lab, Department of Mechanical Engineering, Bilkent University, Çankaya, 06800 Ankara, Turkey. E-mail: gulce.bayram@bilkent.edu.tr, luca@bilkent.edu.tr

<sup>b</sup> Institut für Theoretische Physik II: Weiche Materie, Heinrich-Heine-Universität Düsseldorf, 40225 Düsseldorf, Germany. E-mail: fabian.schwarzendahl@hhu.de, hlowen@hhu.de

<sup>c</sup> Department of Mechanical Engineering, Imperial College London, SW7 2AZ, UK

† Electronic supplementary information (ESI) available: Movies of colloidal suspensions under shear flow. See DOI: <https://doi.org/10.1039/d3sm00035d>





$$\frac{d\theta_i}{dt} = \eta_i(t) + \dot{\gamma}/2. \quad (2)$$

The self-propulsion (or motility) has a constant magnitude of  $v_0$  in the direction of a unit vector  $\mathbf{e}_i = (\cos\theta_i(t), \sin\theta_i(t))$  for particle  $i$ . The orientation angle  $\theta_i$  changes diffusively through  $\eta_i$ , which is a Gaussian white noise with zero mean  $\langle \eta_i(t) \rangle = 0$  and variance  $\langle \eta_i(t)\eta_i(t') \rangle = 2D_r\delta_{ij}\delta(t-t')$ . The rotational diffusion coefficient  $D_r$  controls the strength of the rotational fluctuations. Additionally, the second term on the right-hand side of eqn (2) takes into account the effect of shear on the rotational motion of an isolated particle under shear flow.<sup>38</sup> Hydrodynamic interactions between the colloids are neglected.

The colloidal particles interact *via* a repulsive Yukawa potential

$$U(r_{ij}) = U_0 a \frac{\exp(-\lambda r_{ij}/a)}{r_{ij}}, \quad (3)$$

which is a potential commonly used in the case of charge-stabilized suspensions in two dimensions.<sup>39</sup> The screening parameter  $\lambda$  represents the range of the interaction between two limiting cases: (i) hard-core ( $\lambda \rightarrow \infty$ ) and (ii) unscreened Coulomb ( $\lambda \rightarrow 0$ )<sup>40</sup> interactions. Moreover,  $r_{ij} = |r_i - r_j|$  is the distance between two particle centers,  $a$  is a typical length scale taken as a unit of length determining the screening length as  $a/\lambda$  and  $U_0$  is the bare potential strength. The Gaussian white noise,  $\xi_i$  mimics the stochastic interactions with a thermal bath, with zero mean and variance  $\langle \xi_i(t)\xi_i(t') \rangle = 2D_0\delta_{ij}\delta_{xy}\delta(t-t')$ , where  $D_0$  is the translational diffusion coefficient. The last term in eqn (1) represents the imposed shear in the  $x$  direction ( $\mathbf{e}_x$  is the unit vector pointing into the  $x$  direction) with respect to the position of particle  $i$  along the shear gradient direction  $y$ . Finally,  $\Gamma$  is the friction coefficient.

We perform steady shear simulations for different number densities  $\rho_N = N/\Omega$ , the ratio of number of particles and the system area  $\Omega = L_x L_y$ , with periodic boundary conditions, schematically shown in Fig. 1(a). The dimensions of the rectangular computational box are chosen as  $L_x, L_y = (120a, 104a)$ . Three different numbers of particles  $N = 14\,400, 10\,368$  and  $8\,448$  are used in the simulations corresponding to three different reduced number densities of  $\rho_N a^2 = 0.68, 0.83, 1.15$ . The bare potential strength is fixed to  $U_0 = 800k_B T$  and the simulations are started from a hexagonal crystal configuration of the particles. Further, a soft potential with the screening parameter  $\lambda = 3.5$  is chosen. The time step for the evolution of the particle positions is  $\Delta t = 0.0001\tau_0$ , with the natural unit of time  $\tau_0 = a^2/D_0$ . The colloid–colloid pairwise interactions are cut off at an inter-particle distance of  $2a$  and the rotational diffusion coefficient is  $D_r = 3.5\tau_0^{-1}$ . After an initial relaxation time of  $t = 0.4\tau_0$ , shear is imposed.

## 2.2 Measured quantities

The shear stress, which is the off-diagonal component of the stress tensor, is measured by

$$\sigma_{xy} = -\frac{1}{2\Omega} \sum_{i=1}^N \sum_{i>j} \frac{\partial U}{\partial r_{ij}} \frac{r_{ij}^x r_{ij}^y}{r_{ij}}. \quad (4)$$

Fig. 1 Schematic representations of (a) the sheared active colloidal suspensions (the colour bar represents the distribution of shear force throughout the computational box), (b) the expected particle arrangements in different fluids, (c) shear stress–shear rate curve for different fluids.

intermediate activities it becomes Newtonian and at very high activity it is shear thickening (Fig. 1). The shear thickening behaviour is induced by particle clusters that stem from the active motion of the particles. Therefore we refer to this new phenomenon as motility-induced shear thickening (MIST). In fact, MIST is somehow a consequence of motility-induced phase separation (MIPS)<sup>4,5</sup> in the bulk which shows a pre-clustering in the one-fluid phase even before full phase separation is reached. These clusters are responsible for the shear-thickening under shear. The full rheological response is further well characterized using a Herschel–Bulkley model for the stress as a function of the shear rate, which shows the continuous transition from shear thinning to shear thickening as the activity is increased. Therefore the rheological behaviour can be tuned by activity.

## 2 Simulation method

We study a suspension of  $N$  self-propelled particles moving in two spatial dimensions under shear flow, Fig. 1(a). In Section 2.1, we introduce the model to be used for simulating this system, including the units and parameters used in it. We then describe in Section 2.2 the observables that we measure in our simulation in order to analyse the rheological response of the system for the different self-propulsion and shear forces.

### 2.1 Model

In two spatial dimensions, the over-damped dynamics of the colloids are modeled by active Brownian particles in the presence of a steady shear rate  $\dot{\gamma}$ ,

$$\frac{d\mathbf{r}_i}{dt} = -\frac{1}{\Gamma} \sum_{i<j} \nabla_i U_{ij} + v_0 \mathbf{e}_i + x_i + \dot{\gamma} y_i(t) \mathbf{e}_x, \quad (1)$$



$r_{ij}^x$  and  $r_{ij}^y$  are the distance between the centres of two particles  $i$  and  $j$  in direction of  $x$  and  $y$ , respectively. The stress is nondimensionalised by considering the thermal energy  $k_B T$  and length scale  $a$  as  $\sigma_{xy} a^3 / k_B T$ , where  $k_B$  is the Boltzmann constant and temperature  $T$  with  $k_B T = D_0 \Gamma$  resulting from the near-equilibrium fluctuation–dissipation relation. We note that the definition of shear stress in eqn (4) is the generalization of the passive to the active case and therefore it is some kind of nonequilibrium effective shear stress. The dynamics of the system is controlled by two dimensionless numbers.

(1) First, the imposed shear rate is given by the shear Peclet number,  $Pe_s = \dot{\gamma} a^2 / D_0$ , which measures the ratio of the shear force to thermal fluctuations.

(2) The second dimensionless number is the active Peclet number,  $Pe_a = v_0 a / D_0$ , which measures the ratio between the self-propulsion force (or the motility strength) and thermal fluctuations.

The magnitudes of the dimensionless numbers considered here are  $Pe_a \in [0, 150]$  for the active Peclet number and  $Pe_s \in [0, 40]$  for the shear Peclet number.

The structural changes in the system are monitored by two-dimensional bond orientational order parameters,<sup>41</sup>

$$\psi_\nu = \left| \frac{1}{N} \sum_{i=1}^N \frac{1}{\nu} \sum_{j \in \mathcal{N}(i)} e^{i\nu\theta_{ij}} \right|^2 \quad (5)$$

where  $\mathcal{N}(i)$  is the set of  $\nu$  nearest neighbour particles of the  $i$ th particle and  $\theta_{ij}$  is the angle between the bond vector pointing from particle  $i$  to  $j$  and horizontal fixed axis. For  $\nu = 6$  the order parameter is the hexatic order parameter  $\psi_6$ , which is close to zero in the disordered phase whereas it equals 1 in a perfect hexagonal crystal. Similarly, we also analyse the tetratic orientational order by using  $\psi_4$ .

## 3 Results

### 3.1 Melting by the combined action of shear and activity

Our particular interest is the characterization of self-propelled particles in the dense regime,  $\rho_N a^2 = 1.15$ . We first analyze the instantaneous shear–stress–relation, *i.e.* the relation between  $\sigma_{xy}$  and the imposed strain ( $\gamma = \dot{\gamma}t$ ), at a constant shear rate  $Pe_s = 20$  for different self-propulsions. In parallel, we also monitor the bond-orientational order parameters of the system. We note that the results represented here show the system behaviour starting immediately from the time we impose the shearing force ( $t = 0.4\tau_0$ ).

In the absence of particle motility ( $Pe_a = 0$ ), the system starting out of the perfect hexagonal crystal stays in this solid-like phase during the relaxation, as documented in Fig. 2 snapshot(1). When shearing is turned on thereafter, shear stress starts building up to a peak value, *i.e.*, point (2) in Fig. 2(a) which brings the system to the onset of melting. At this point, the system is not disordered yet and we discuss this structural transition in detail later on. Here, this nearly linear increase in the shear stress represents that the system response is nearly elastic at low strains. Further accumulation of the strain melts the crystal and, accordingly, causes a release of stress due to structural relaxation. This brings the system to a strain-independent plateau at higher strains. We can associate this best with the shear-induced disordering transition where the equilibrium melting transition is displaced by the imposed shear rate.<sup>42–44</sup>

Moreover, the self-propulsion helps to cause a preliminary melting, which appears as a decrease in  $\psi_6$  during the relaxation of the system. This fastens the hexagonal–liquid transition and consequently decreases the stress barrier, which is defined by the shear stress peak. Much higher activities ( $Pe_a \geq 30$ ) melt the crystal entirely even before imposing the shear rate, thereby annihilating the stress barrier. After that, the colloidal suspension is disordered and its behaviour is liquid-like [in Fig. 2

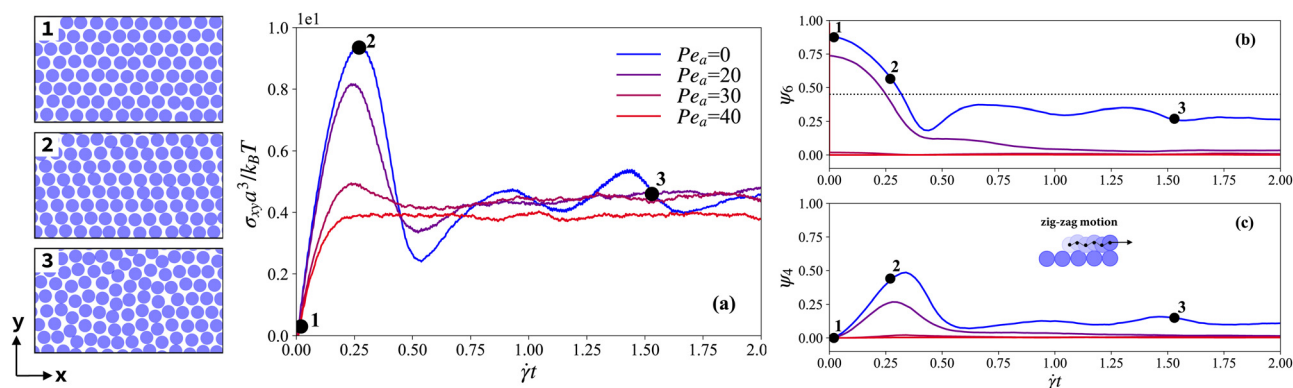


Fig. 2 (Left) Snapshots of particle configurations for (1) solid-like, (2) cubic-like and (3) liquid-like phases of the passive system, in which the system conditions correspond to the numbered black dots in the plots: (a) the instantaneous shear stress ( $\sigma_{xy}$ ) with respect to strain ( $\gamma = \dot{\gamma}t$ ) for passive ( $Pe_a = 0$ ) and active systems ( $Pe_a > 0$ ) at a constant shear rate  $Pe_s = 20$ . The corresponding structural changes throughout the bond orientational order parameters,  $\psi_6$  (b) and  $\psi_4$  (c). The black dotted–horizontal line defines the position of structural transition for the hexagonal configuration,  $\psi_6 \approx 0.45$ .<sup>14</sup> The inset in (c) shows the representation of the zig-zag motion of a colloidal particle under shear. A colloidal particle follows a zig-zag-like trajectory (black dashed line) while moving to the right direction over the particle layer underneath due to the imposed shear.



snapshot(3)]. In the latter case, the equilibrium melting transition is significantly displaced by self-propulsion and melting is thus expected for the parameters used to define the colloidal interactions.<sup>14,45–47</sup>

Points (2) in Fig. 2(a) and (b) together reveal that the stress peak appears just before the drop of  $\psi_6$  below the structural transition,  $\psi_6 = 0.45$ .<sup>14</sup> In fact, the solid-to-liquid transition is not direct throughout this barrier but rather occurs *via* a structural rearrangement [Fig. 2 snapshot(2)]. The zigzag motion of the particles, which emerges by their alternating motion in one layer between filling the grooves of the next layer and hopping up from there,<sup>48,49</sup> temporarily gives a rise in  $\psi_4$  [see Fig. 2(c)]. We might expect this increase of  $\psi_4$  at first sight when we look at the arrangement of particles in the snapshot (2). Additionally, even in the liquid regime below  $\psi_6 < 0.45$ , where the shear melts the crystal as a whole, some ordered regions show up at times due to this zig-zag motion of the particles in subsequent layers [see the ESI,† Movie\_Passive\_Pes20.mp4]. This is similar to what was observed by Wu *et al.*<sup>50</sup> in melting passive colloidal suspensions under shear. Although these ordered structures give rise to local increases in the hexagonal order parameter in the passive system below the structural transition line [see Fig. 2(b)], the self-propulsion destroys these local ordered structures, resulting in zero  $\psi_6$ .

Furthermore, we see that the subsequent melting first starts with local disruptions of the ordered structures, similar to the so-called interstitial defects<sup>44</sup> observed in purely shear-induced

disordering. For the passive suspension at the shear rate  $Pe_s = 20$ , we see that the suspension is able to restore the defect at one region while creating another one at another region. Therefore, the defects are not able to grow and the system stays in a solid-like regime. On the other hand, in an active suspension the interstitial defects can grow and spread around the domain due to the effect of self-propulsion [see the comparison with the defects in the passive suspension using Voronoi diagrams in the ESI,† Fig. S1], resulting at the end in the enhanced melting of the system [see the ESI,† (i) Section 1.2 and (ii) Movie\_Pea20\_interstitialdefects.mp4].

### 3.2 Motility-induced shear thickening (MIST) and shear thinning

We now consider the liquid regime and discuss the time-averaged shear stress  $\bar{\sigma}_{xy}$  with respect to the imposed shear rate  $\dot{\gamma}$  [see in Fig. 3(a)], which yields the rheology of the active colloidal suspensions. Note that the shear stress data are time averaged over the steady state time frame corresponding to the strain-independent plateau of the stress and the minimum shear rate is  $Pe_s = 1$  in Fig. 3(a).

We use the common Herschel–Bulkley model<sup>51</sup> to quantify the possible non-Newtonian behaviour where  $\sigma_{xy} = \sigma_0 + K\dot{\gamma}^n$  with  $\sigma_0$  representing the yield stress. A shear thinning liquid is characterized by power indexes  $n < 1$ , while for a shear thickening liquid  $n > 1$ . As a special case,  $n = 1$  represents the classical Newtonian liquid. In Fig. 3(b) we fit our stress–shear

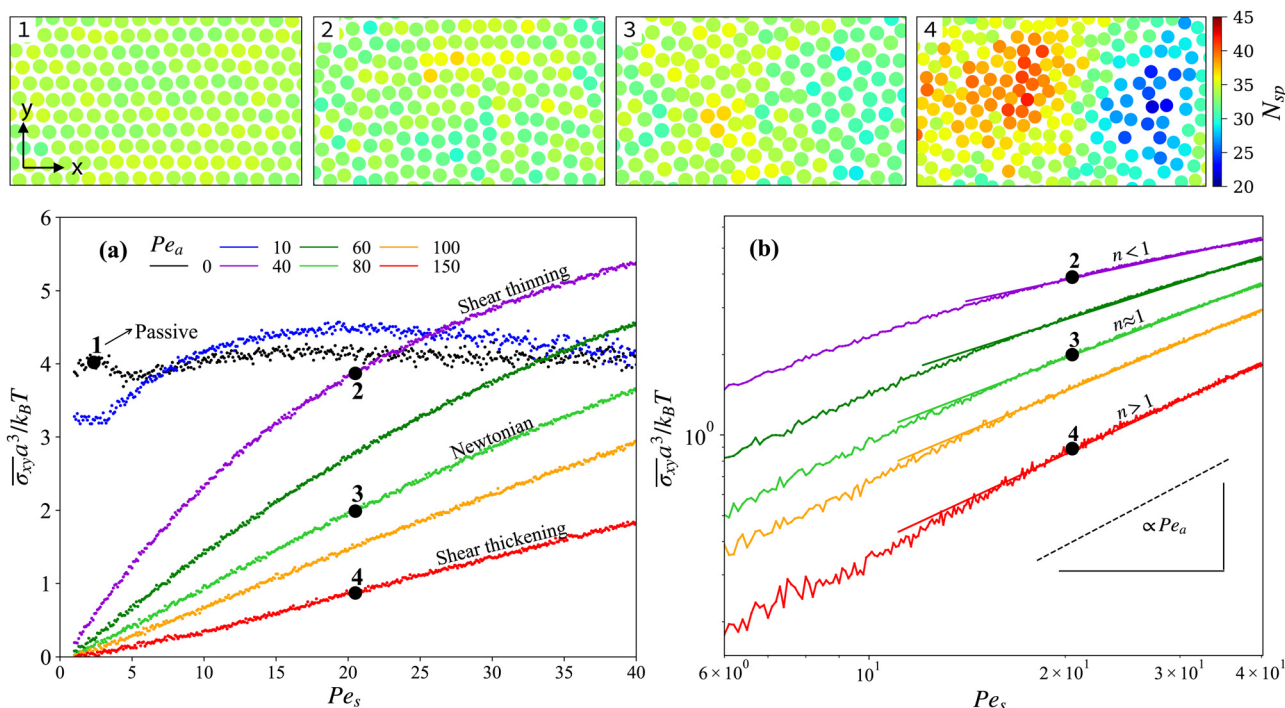


**Fig. 3** (Top) Snapshots of particle configurations: (1) solid-like, (2) shear-thinning, (3) Newtonian and (4) shear-thickening, where the particles are coloured with respect to their number of surrounding particles ( $N_{sp}$ ). (a) Nondimensional shear stress  $\bar{\sigma}_{xy}$  – shear rate  $\dot{\gamma}$  curves for  $Pe_s \geq 1$  at different self-propulsion forces. (b) Liquid-like regime shown in log–log scale where the Herschel–Bulkley model fitting has been applied is indicated by the fitting lines for different rheological behaviours with respect to the corresponding power indexes ( $n$ ). The numbered black dots represent the conditions of the simulations where the snapshots are taken. The corresponding viscosity curves are shown in the ESI,† Section 1.4.



rate simulation data for different activities to this model. Thereby, we explore the effect of the self-propulsion on the rheological response of the system. Here, we analyse the active colloidal suspensions starting with  $Pe_a \geq 40$  where the suspension is entirely in a liquid phase with  $\psi_6 = 0$ . For the passive and low activity (*i.e.*,  $Pe_a = 10$ ) cases, the suspension has still local crystals meaning that  $\psi_6$  cannot reach zero [see the ESI,† Section 1.3 and Fig. S2]. In these cases, we cannot apply the Herschel–Buckley model if  $\psi_6 > 0$  since the rheology of the suspension becomes more complex, allowing plateau or non-monotonic behaviour in the shear stress *versus* strain rate curve. Moreover we follow up the structural changes by the number of surrounding particles  $N_{sp}$ , which is the number of particles counted inside the surrounding circle with a radius  $r_{surr}/a = 3$  for every particle individually [see the top snapshots in Fig. 3]. In this way, we better distinguish the occurrence of clustering and, accordingly, the onset of shear thickening in the system with increasing self-propulsion strength.

The passive system, initially in the crystalline phase, does not melt at very low shear rates ( $Pe_s < 2.5$ ) and shows solid-like behaviour [Fig. 3(1)] with non-zero yield stress  $\bar{\sigma}_0 a^3/k_B T \approx 4$ , see Fig. 3(a). This is in line with what Chen and Zukoski demonstrated for passive ordered suspensions.<sup>48</sup> Here, thermal fluctuations are responsible for the motion of colloids. At this solid regime, we see that turning on the activity diminishes the yield stress. In addition to weak activities, the hexagonal order in the system can be destroyed by more effective shearing, above the so-called critical shear rate.<sup>44,52</sup> However, we note that in these weak activities, the phase transition of the suspension is not fully completed because shear can also induce ordering, which is known as a flow-induced crystallization phenomenon in colloidal suspensions.<sup>53,54</sup> On the other hand, activities  $Pe_a > 30$  eliminate the solid-like behaviour giving  $\bar{\sigma}_0 = 0$ , since the hexatic-to-liquid transition is already reached by activity [see again in Fig. 2(b)]. Thereafter, the resulting melt starts behaving as a shear-thinning liquid which is a non-Newtonian behaviour characterized by the slopes lower than 1 ( $n < 1$ ), see point (2) in Fig. 3(b). Here, the shear force has control over the motion of the particles and yields sliding layers of particles aligned in the direction of shear flow [snapshot 2 in Fig. 3]. Indeed, this layered flow, which is also discussed in Section 3.1, has been previously found as being intrinsic to the shear thinning behaviour of passive Brownian colloidal suspensions.<sup>48,55,56</sup> Moreover, local ordered regions are temporarily observed as a result of the zig-zag motion of colloids, which is also a shear-induced ordering phenomenon seen in 2D shear-thinning colloidal suspensions.<sup>57</sup> Although the shear thinning behaviour is relatively well understood in Brownian colloidal systems, the effect of self-propulsion has not been addressed. We observe that activities up to  $Pe_a \approx 80$  assist only the shear in melting the system, while the resulting melt maintains the same shear-thinning behaviour observed for passive suspensions [see the ESI,† Movie\_shear thinning.mp4].

Interestingly, we find that increasing the self-propulsion force triggers the rheological response of the suspension and changes qualitatively the behaviour albeit in a smooth way. At moderate motilities,  $Pe_a \approx 90$ , the fluid behaviour is not

shear-thinning, but Newtonian, corresponding to the curves (3) with an exponent  $n = 1$  in Fig. 3(a) and (b). In this regime, self-propulsion degrades the stability of layered flow and the suspension becomes completely disordered, see snapshot (3) in Fig. 3, [also see the ESI,† Movie\_Newtonian.mp4]. Similar to the mechanism discussed in Section 3.1, some of the interstitial defects appeared in the shear-thinning liquid which spread with increasing self-propulsion, being responsible for the loss of thinning.

Above  $Pe_a \approx 100$ , we observe that the self-propulsion starts dominating over shear and reveals structural heterogeneities in the system, leading to transient cluster formation as shown by the snapshot (4) in Fig. 3, [also see the ESI,† Movie\_shear thickening.mp4]. In this case, the slope of shear stress–shear rate curves exceeds 1 [see (4) in Fig. 3(b)], meaning that the suspension changes crossover from Newtonian to shear thickening behaviour. Here, we also observe that the colloidal suspension starts showing clusters even before imposing a shear to the system, which is expected for active particles in this parameter regime<sup>58</sup> [see the ESI,† at the beginning of Movie\_shear thickening.mp4 in the absence of shear]. However, we found that these clusters enable the system to behave as a shear-thickening fluid when the system is forced to flow. Therefore, we refer to this behaviour as motility-induced shear thickening (MIST) in some analogy to motility-induced phase separation (MIPS). In fact, the cluster formation generating MIST is a precursor of MIPS, which has been seen starting at a critical self-propulsion of about  $Pe_{a,cr} \approx 90$ . Additionally, especially for this behaviour, we observe visually that the number of surrounding particles  $N_{sp}$  remarkably differs from region to region in the system [see snapshot (4) in Fig. 3].

The shear thinning-to-thickening transition has been attained for years in passive colloidal suspensions with very high shear rates ( $Pe_s > 100$ ), by underlining similar cluster formations in the shear-thickening fluid due to the hydrodynamic interactions and lubrication forces.<sup>49,59–61</sup> In this study, instead, we could reach this transition by keeping the range of shear rate constant at relatively low values, while increasing the activity of colloids, with neglecting hydrodynamic interactions. In this work, the cluster formation is not triggered by shearing extremely the system, rather it is triggered by motility.

### 3.3 The effect of particle density

Next, we analysed the stress–shear rate curves for the suspensions with two lower particle densities, a semi-dilute suspension  $\rho_N a^2 = 0.83$ , and a dilute suspension  $\rho_N a^2 = 0.68$ , respectively, achieved by lowering the number of particles in the simulation box while keeping all other parameters the same. Obviously, lowering the density creates more disorder in general. Thus, the solid behaviour is found as limited to very small parameter ranges. Consequently, a dilute suspension shows lower yield stresses compared to the dense case at the same activities [see the ESI,† Section 1.5]. Accordingly, the system starts showing a shear thinning behaviour even with very low self-propulsion forces. Fig. 4 summarizes the trend of the power index  $n$  with



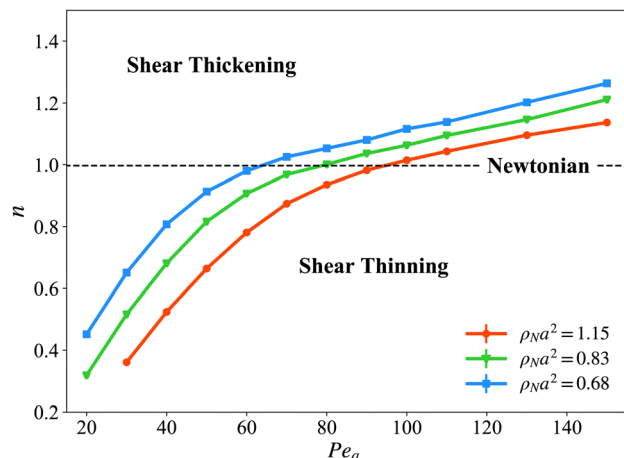


Fig. 4 The power index  $n$  vs. the active Peclet number  $Pe_a$  for different particle densities. The horizontal dashed line corresponds to the Newtonian case with a slope of 1 on a log–log scale.

increasing self-propulsion for all cases. Here, again, the exponents are obtained by fitting the shear stress/shear rate data to the power law model for these two other densities, as done for the dense system in Section 3.2. The red line in this figure, which corresponds to the dense suspension case, starts at  $Pe_a \approx 30$ , since the system retains mostly solid-like behaviour below this value, followed by shear-induced disordering with increasing activity.

Regarding the liquid-like regime, it is evident that the critical self-propulsion ( $Pe_{a,cr}$ ) for the shear thinning to thickening transition shifts to lower activities with decreasing particle density. In other words, dilute suspensions can thicken easier than dense ones. The underlying reason for this effect can be intuitively related to clustering. Keeping the particles very close to each other, as in a dense system, obviously pronounces their collisions. Therefore, possible cluster formation becomes difficult in the system. Although some clusters are formed with these activities, they are not stable enough, such that they can be damaged by any strike from other particles around them. However, increasing the self-propulsion further promotes clustering and finally brings the system into a thickening regime. As we discussed previously, activity triggers the colloidal suspension to behave as a shear-thickening fluid. Conversely, active colloids in a dilute environment can constitute more stable clusters even with low self-propulsion due to fewer repulsive collisions coming from particles around the clusters, accordingly undergoing this thinning-to-thickening transition earlier [see Fig. 4].

This scenario is also confirmed by Fig. 5, where we report the standard deviation of the time averaged number of surrounding particles

$$\sigma_{\overline{N}_{sp}} = \sqrt{\frac{1}{N} \sum_{i=1}^N (\overline{N}_{sp,i} - \langle \overline{N}_{sp} \rangle)^2} \quad (\text{in which}$$

$\langle \overline{N}_{sp} \rangle = \frac{1}{N} \sum_{i=1}^N \overline{N}_{sp,i}$ ) vs. the active Peclet number  $Pe_a$  for the three different densities. Here, to quantify the cluster formation in the liquid regime, we use  $N_{sp}$  since the parameters  $\psi_4$  and  $\psi_6$  are more connected to the ordered structures of the

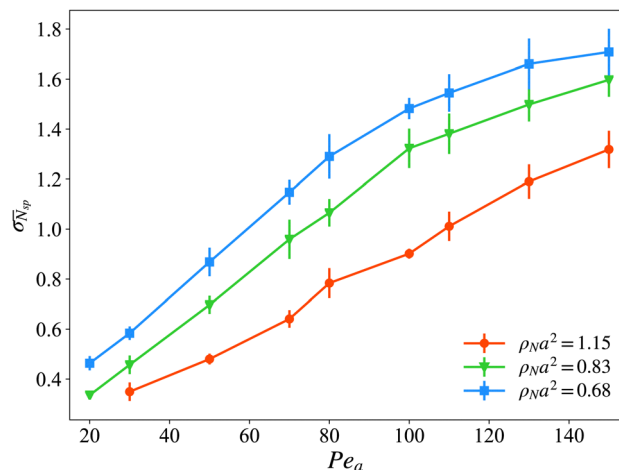


Fig. 5 Standard deviation of the time averaged number of surrounding particles,  $\sigma_{\overline{N}_{sp}}$ , vs. the active Peclet number  $Pe_a$  for different particle densities,  $\rho_N a^2 = 1.15$  (circle),  $\rho_N a^2 = 0.83$  (triangle) and  $\rho_N a^2 = 0.68$  (square) at  $Pe_s = 30$ .

solid crystals. Typically there are more fluctuations in the surrounding particle density for dilute systems, also for weak self-propulsion forces. However, here the activity enhances dramatically (i) the local density inhomogeneities, as revealed by the strong increase of  $\sigma_{\overline{N}_{sp}}$  with  $Pe_a$ , and (ii) the gap in  $\sigma_{\overline{N}_{sp}}$  between dilute and dense systems. The motility-induced local density inhomogeneities correspond to pre-clustering which provides evidence that this is the underlying reason for the shear-thickening behaviour consistent with snapshot (4) in Fig. 3. Since this pre-clustering is more pronounced for dilute systems, the MIST transition occurs earlier in these systems confirming our previous intuitive explanation.

## 4 Conclusions

In this work, we have explored the effect of self-propulsion on the rheological response of the dense colloidal suspensions under steady shear by using Brownian dynamics simulations. First, the solid-to-liquid transition of the suspension was characterized, showing that activity helps to melt the systems, as shown before in literature.<sup>14,62</sup> When melting, the self-propulsion of the colloids reduces the stress barrier that the system has to overcome in order to transition from the solid to the liquid state. Self-propulsion is not only responsible for assisting the shear in melting the colloidal suspension but also introduces a transition in the rheology of the melted suspension. Depending on the activity of colloids in the suspension, different fluid behaviours are found: shear thinning, Newtonian and shear-thickening. The underlying reason behind this response is a well-known dynamical mechanism of active colloidal particles: activity-induced clustering. When the self-propulsion is sufficiently strong to prevail against the shear, or even before shearing, a cluster formation is observed. The existence of these clusters creates additional resistance to flow when the suspension is exposed to shear, causing it to behave



as a shear-thickening fluid. We referred to this as motility-induced shear-thickening in this article.

The shear-thinning to thickening transition reported here is different from the transition observed in passive colloidal systems. Passive colloids tend to stick together by hydrodynamic and lubrication forces at high shear rates,<sup>60,63</sup> while active colloids cluster due to their motility (akin to motility-induced phase separation). The simulations presented here were performed in the absence of hydrodynamic interactions. Including hydrodynamics and lubrication forces would be an interesting future avenue since hydrodynamics suppress the tendency for active particles to form clusters,<sup>64–66</sup> while on the other hand, hydrodynamics lead to clusters of sheared passive colloids. Additionally, the rheological behaviour of the colloidal suspension at low activities is very promising and requires more detailed analyses with possibly using constitutive relationships more complex than Hershel–Buckley. Further, it would be interesting to test the response in a three-dimensional set-up or to include inertia to the active particles motion.<sup>67,68</sup> Experimentally, the shear thinning to thickening transition could be tested using active colloids in a “washing-machine” set up.<sup>69</sup> Finally, it would be interesting to extend our simulation to particles of more complex shape than spheres such as active polymers or active filaments,<sup>70,71</sup> where new rheological behaviour due to active entanglements can be expected in dense solutions.

## Conflicts of interest

There are no conflicts to declare.

## Acknowledgements

We thank Jürgen Horbach for helpful discussions. The work of A. G. B. was supported within the EU MSCA-ITN ActiveMatter (proposal no. 812780).

## Notes and references

- M. C. Marchetti, J.-F. Joanny, S. Ramaswamy, T. B. Liverpool, J. Prost, M. Rao and R. A. Simha, *Rev. Mod. Phys.*, 2013, **85**, 1143.
- S. Ramaswamy, *Annu. Rev. Condens. Matter Phys.*, 2010, **1**, 323–345.
- C. Bechinger, R. Di Leonardo, H. Löwen, C. Reichhardt, G. Volpe and G. Volpe, *Rev. Mod. Phys.*, 2016, **88**, 045006.
- I. Buttinoni, J. Bialké, F. Kümmel, H. Löwen, C. Bechinger and T. Speck, *Phys. Rev. Lett.*, 2013, **110**, 238301.
- J. Palacci, S. Sacanna, A. P. Steinberg, D. J. Pine and P. M. Chaikin, *Science*, 2013, **339**, 936–940.
- A. Bricard, J.-B. Caussin, D. Das, C. Savoie, V. Chikkadi, K. Shitara, O. Chepizhko, F. Peruani, D. Saintillan and D. Bartolo, *Nat. Commun.*, 2015, **6**, 7470.
- S. M. Mousavi, I. Kasianiuk, D. Kasyanyuk, S. K. Velu, A. Callegari, L. Biancofiore and G. Volpe, *Soft Matter*, 2019, **15**, 5748–5759.
- N. Narinder, J. R. Gomez-Solano and C. Bechinger, *New J. Phys.*, 2019, **21**, 093058.
- G. Volpe, I. Buttinoni, D. Vogt, H.-J. Kümmerer and C. Bechinger, *Soft Matter*, 2011, **7**, 8810–8815.
- C. Maggi, J. Simmchen, F. Saglimbeni, J. Katuri, M. Dipalo, F. De Angelis, S. Sanchez and R. Di Leonardo, *Small*, 2016, **12**, 446–451.
- N. Klongvessa, F. Ginot, C. Ybert, C. Cottin-Bizonne and M. Leocmach, *Phys. Rev. E*, 2019, **100**, 062603.
- G. Briand, M. Schindler and O. Dauchot, *Phys. Rev. Lett.*, 2018, **120**, 208001.
- G. Briand and O. Dauchot, *Phys. Rev. Lett.*, 2016, **117**, 098004.
- J. Bialké, T. Speck and H. Löwen, *Phys. Rev. Lett.*, 2012, **108**, 168301.
- S. Henkes, Y. Fily and M. C. Marchetti, *Phys. Rev. E: Stat., Nonlinear, Soft Matter Phys.*, 2011, **84**, 040301.
- N. de Macedo Biniossek, H. Löwen, T. Voigtmann and F. Smallenburg, *J. Phys.: Condens. Matter*, 2018, **30**, 074001.
- L. M. C. Janssen, *J. Phys.: Condens. Matter*, 2019, **31**, 503002.
- R. Ni, M. A. C. Stuart and M. Dijkstra, *Nat. Commun.*, 2013, **4**, 2704.
- R. Mandal and P. Sollich, *Proc. Natl. Acad. Sci. U. S. A.*, 2021, **118**, e2101964118.
- A. Sokolov and I. S. Aranson, *Phys. Rev. Lett.*, 2009, **103**, 148101.
- J. Gachelin, G. Mino, H. Berthet, A. Lindner, A. Rousselet and É. Clément, *Phys. Rev. Lett.*, 2013, **110**, 268103.
- H. M. López, J. Gachelin, C. Douarche, H. Auradou and E. Clément, *Phys. Rev. Lett.*, 2015, **115**, 028301.
- Z. Liu, K. Zhang and X. Cheng, *Rheol. Acta*, 2019, **58**, 439–451.
- V. A. Martinez, E. Clément, J. Arlt, C. Douarche, A. Dawson, J. Schwarz-Linek, A. K. Creppy, V. Škultéty, A. N. Morozov and H. Auradou, *et al.*, *Proc. Natl. Acad. Sci. U. S. A.*, 2020, **117**, 2326–2331.
- S. Rafa, L. Jibuti and P. Peyla, *Phys. Rev. Lett.*, 2010, **104**, 098102.
- T. Ishikawa and T. Pedley, *J. Fluid Mech.*, 2007, **588**, 399–435.
- B. M. Haines, A. Sokolov, I. S. Aranson, L. Berlyand and D. A. Karpeev, *Phys. Rev. E: Stat., Nonlinear, Soft Matter Phys.*, 2009, **80**, 041922.
- D. Saintillan, *Exp. Mech.*, 2010, **50**, 1275–1281.
- S. D. Ryan, B. M. Haines, L. Berlyand, F. Ziebert and I. S. Aranson, *Phys. Rev. E: Stat., Nonlinear, Soft Matter Phys.*, 2011, **83**, 050904.
- M. Moradi and A. Najafi, *EPL*, 2015, **109**, 24001.
- T. M. Bechtel and A. S. Khair, *Rheol. Acta*, 2017, **56**, 149–160.
- H. Hayano and A. Furukawa, *Phys. Rev. Lett.*, 2022, **4**, 043091.
- M. Cates, S. Fielding, D. Marenduzzo, E. Orlandini and J. Yeomans, *Phys. Rev. Lett.*, 2008, **101**, 068102.
- Y. Hatwalne, S. Ramaswamy, M. Rao and R. A. Simha, *Phys. Rev. Lett.*, 2004, **92**, 118101.
- L. Giomi, T. B. Liverpool and M. C. Marchetti, *Phys. Rev. E: Stat., Nonlinear, Soft Matter Phys.*, 2010, **81**, 051908.



- 36 A. Loisy, A. P. Thompson, J. Eggers and T. B. Liverpool, *J. Chem. Phys.*, 2019, **150**, 104902.
- 37 B. Liebchen and H. Löwen, *J. Chem. Phys.*, 2019, **150**, 061102.
- 38 J. K. Dhont, *An Introduction to Dynamics of Colloids*, Elsevier, 1996.
- 39 H. Löwen, *J. Phys.: Condens. Matter*, 1992, **4**, 10105.
- 40 H. Löwen and G. Szamel, *J. Phys.: Condens. Matter*, 1993, **5**, 2295.
- 41 P. J. Steinhardt, D. R. Nelson and M. Ronchetti, *Phys. Rev. B: Condens. Matter Mater. Phys.*, 1983, **28**, 784.
- 42 B. J. Ackerson and N. A. Clark, *Phys. Rev. Lett.*, 1981, **46**, 123.
- 43 P. Holmqvist, M. Lettinga, J. Buitenhuis and J. K. Dhont, *Langmuir*, 2005, **21**, 10976–10982.
- 44 S. Butler and P. Harrowell, *J. Chem. Phys.*, 1995, **103**, 4653–4671.
- 45 J. U. Klamser, S. C. Kapfer and W. Krauth, *Nat. Commun.*, 2018, **9**, 5045.
- 46 L. Berthier, *Phys. Rev. Lett.*, 2014, **112**, 220602.
- 47 Y. Fily, S. Henkes and M. C. Marchetti, *Soft Matter*, 2014, **10**, 2132–2140.
- 48 L. Chen and C. Zukoski, *Phys. Rev. Lett.*, 1990, **65**, 44.
- 49 R. L. Hoffman, *J. Rheol.*, 1998, **42**, 111–123.
- 50 Y. L. Wu, D. Derks, A. van Blaaderen and A. Imhof, *Proc. Natl. Acad. Sci. U. S. A.*, 2009, **106**, 10564–10569.
- 51 P. Saramito, *Complex fluids*, Springer, 2016.
- 52 S. Butler and P. Harrowell, *Phys. Rev. E: Stat., Nonlinear, Soft Matter Phys.*, 1995, **52**, 6424.
- 53 L. T. Shereda, R. G. Larson and M. J. Solomon, *Phys. Rev. Lett.*, 2010, **105**, 228302.
- 54 L. T. Shereda, R. G. Larson and M. J. Solomon, *Korea Aust. Rheol. J.*, 2010, **22**, 309–316.
- 55 L. Chen, B. Ackerson and C. Zukoski, *J. Rheol.*, 1994, **38**, 193–216.
- 56 G. Wilemski, *J. Stat. Phys.*, 1991, **62**, 1239–1253.
- 57 B. J. Ackerson and P. Pusey, *Phys. Rev. Lett.*, 1988, **61**, 1033.
- 58 P. Digregorio, D. Levis, A. Suma, L. F. Cugliandolo, G. Gonnella and I. Pagonabarraga, *Phys. Rev. Lett.*, 2018, **121**, 098003.
- 59 G. Bossis and J. Brady, *J. Chem. Phys.*, 1989, **91**, 1866–1874.
- 60 E. Brown and H. M. Jaeger, *Rep. Prog. Phys.*, 2014, **77**, 046602.
- 61 T. Lorenzo and L. Marco, *J. Colloid Interface Sci.*, 2022, **624**, 637–649.
- 62 S. Li, H. Jiang and Z. Hou, *Soft Matter*, 2015, **11**, 5712–5718.
- 63 N. J. Wagner and J. F. Brady, *Phys. Today*, 2009, **62**, 27–32.
- 64 R. M. Navarro and S. M. Fielding, *Soft Matter*, 2015, **11**, 7525–7546.
- 65 M. Theers, E. Westphal, K. Qi, R. G. Winkler and G. Gompper, *Soft Matter*, 2018, **14**, 8590–8603.
- 66 R. Matas-Navarro, R. Golestanian, T. B. Liverpool and S. M. Fielding, *Phys. Rev. E: Stat., Nonlinear, Soft Matter Phys.*, 2014, **90**, 032304.
- 67 C. G. Wagner, M. F. Hagan and A. Baskaran, *Phys. Rev. E*, 2019, **100**, 042610.
- 68 H. Löwen, *J. Chem. Phys.*, 2020, **152**, 040901.
- 69 I. Williams, E. C. Oğuz, H. Löwen, W. C. Poon and C. P. Royall, *J. Chem. Phys.*, 2022, **156**, 184902.
- 70 A. Kaiser, S. Babel, B. ten Hagen, C. von Ferber and H. Löwen, *J. Chem. Phys.*, 2015, **142**, 124905.
- 71 R. G. Winkler and G. Gompper, *J. Chem. Phys.*, 2020, **153**, 040901.

